Raman Induced Avoided Crossings in Adiabatic Optical Potentials: Observation of λ/8 Spatial Frequency in the Distribution of Atoms

R. Gupta, J.J. McClelland and R.J. Celotta
Electron Physics Group
National Institute of Standards and Technology
Gaithersburg, MD 20899

P. Marte
Physics Department
Harvard University
Cambridge, MA 02138

Abstract

Chromium atoms traverse an optical potential and the resulting spatial distribution is measured by a new method. Atoms are collected on a substrate and an atomic force microscope is used to determine the flux as a function of position. An unexpectedly high spatial frequency ($\lambda/8$) is found in the the atomic distribution. This is attributed to avoided crossings arising from Raman coherences induced between magnetic sublevels. These results show that level crossings and nonadiabatic transitions can play an important role in the manipulation of atomic trajectories by near-resonant light fields.

PACS: 32.80.Pj, 42.50.Vk

The interaction of atoms with near-resonant optical standing waves results in spatially varying optical potentials. The force experienced by the atoms due to such potentials can be used to manipulate atomic motion in a number of ways. For example, as the atoms move along these potentials, the dissipation due to the irreversible process of spontaneous emission can be used to damp the atomic motion and, thereby, create a collimated beam, or a cold, localized sample of atoms [1]. In the absence of spontaneous emission, e.g., in a far-off-resonant standing wave, the conservative motion in these potentials can be used to focus or diffract atoms [2]. These effects have made possible a wide variety of applications, including precision atomic clocks [3], atomic interferometry [4] and nanostructure fabrication [5].

The desire for even more complete control of atomic motion demands a deeper understanding of the basic interaction of atoms with near-resonant light fields. Insight has been gained by studying the spatial distribution of the atoms on the sub-optical wavelength scale. The spatial distribution can be inferred from various spectroscopic observations such as Lamb-Dicke narrowing in the resonance fluorescence spectrum [6] and absorption spectrum [7], absorption in the presence of a non-resonant standing wave [8], Raman transitions in spatially varying potentials [9], and Bragg scattering from an optical lattice [10].

In this Letter we report on a new, direct approach to the study of sub-wavelength atomic spatial distributions. We determine the spatial distribution of Cr atoms in an optical field generated by counter-propagating, orthogonally-linearly polarized (*lin $\perp$ lin*) travelling waves. We use a high-resolution technique where an atomic force microscope is used to determine the flux of atoms deposited on a substrate. With this method, we observe, for the first time, spatial distributions that have a $\lambda/8$ component to their periodicity, where λ is the wavelength of the

light field. We show, through qualitative arguments and also detailed calculations, that this component is a direct result of dynamical focusing in the adiabatic optical potentials of the multilevel Cr atoms, as influenced by Raman coherences. We begin with a discussion of the observed $\lambda/8$ periodicity in terms of level crossings in the optical potentials. We then describe the experimental results, and finally present a detailed quantum Monte-Carlo calculation corresponding to the experiments.

The optical field present in a *lin* $\perp$ *lin* polarization configuration can be decomposed into two circularly-polarized standing waves of opposite polarization whose nodes are spatially displaced by $\lambda/4$. For a multilevel atom such as Cr with $J_g = 3$ and $J_e = 4$ on the ${}^7S_3 \rightarrow {}^7P_4{}^o$ transition, each of the magnetic sublevels of the ground state experiences a light shift (AC stark shift) that has contributions from each of these two standing waves. Because of Clebsch-Gordan coefficients, the negative *M*-sublevels have light-shift potentials most strongly influenced by the σ^- standing wave, and the positive *M*-sublevels have potentials dominated by the σ^+ standing wave. If there is no coupling between the levels, then the potentials are referred to as diabatic, and they have minima at the nodes of the associated dominant standing wave. However, there exists a coherent coupling between magnetic sublevels due to multiphoton Raman transitions which involve absorption of a photon from σ^+ standing wave and stimulated emission into the σ^- standing wave or vice-versa. As a result of this Raman coupling, crossings of the diabatic potentials become avoided crossings. These avoided crossings lead to new local minima in the potentials that also have a periodicity of $\lambda/4$, but are offset from the original minima by $\lambda/8$. It is these new minima that give rise to the $\lambda/8$ component in the observed periodicity of the deposited lines.

To see the effect of the coherent coupling between *M*-sublevels on the potentials of the system, a diagonalization of the Hamiltonian must be carried out. Treating the external degrees of freedom (i.e., position) as a parameterization, rather than treating the full dynamics, leads to a set of adiabatic potentials in the diagonalized basis [11] These potentials are plotted for Cr in Fig. 1; since there is no optical component with π-polarization in the *lin* $\perp$ *lin* configuration, the Raman coupling only exists between magnetic states with $|\Delta M| = 2$, and the potentials are grouped into two independent families associated with odd and even magnetic states (Fig. 1 top and bottom, respectively). In each family, only the top level (labeled *1* for the odd family and *2* for the even family) has the necessary minimum locations, associated with avoided crossings, to generate the $\lambda/8$ component.

While the existence of the extra minima in the optical potentials suggests a cause for the high spatial frequency in the atomic distribution, it is necessary to carefully consider several effects before drawing any conclusions about the prominence of such features. First, since there are several differently-shaped potentials, only some of which have minima at the correct locations, the visibility of the $\lambda/8$ patterns depends on the distribution of the initial population among the various adiabatic eigenstates of the atom. But more important, it must be recognized that nonadiabatic transitions [12] in the avoided crossings due to motional coupling could in principle be very significant. If the nonadiabatic transition probability is high enough, there will be no concentration of atoms at the $\lambda/8$ locations, because the atoms will pass onto the adjacent potential and not be localized.

Although a full dynamical calculation, which is discussed below, must be performed to determine the precise behavior, some qualitative understanding of the role played by nonadiabatic

transitions can be had by considering the shape of the adiabatic potentials. Because the nonadiabatic transition probability is proportional to the velocity of the atoms at the anti-crossing, and inversely proportional to the energy separation between the potential curves [12], the ratio of the kinetic energy and this energy separation gives a qualitative measure for the adiabaticity. Ignoring any initial kinetic energy, this ratio can be approximated by the ratio of the potential well depths to their energy separation. With this criterion it is easy to see from Fig. 1 that the atoms entering potential *1* are quite likely to make a nonadiabatic transition, whereas the atoms in potential *2* are less likely to do so.

Another effect that plays a significant role is the shape of the potential minimum. Most efficient focusing of atoms is achieved with a quadratic minimum [5], which is more closely approximated when the Raman coupling is strong and the level separation is large. Thus, again, atoms travelling on potential *2* would tend to contribute more localized peaks than potential *1*.

Our experimental approach relies on the fact that, because of their low surface mobility [13,14], the spatial distribution of Cr atoms in an optical field can be faithfully captured by inserting a substrate into the field and allowing the atoms to deposit. Most of our setup has been described in detail elsewhere [15] and is only briefly mentioned here. It consists of an effusive source of chromium atoms from a commercial MBE evaporation cell operating at 1650 °C, a precollimating aperture, a region of optical collimation in which dissipative light forces are used to transversely cool the atom beam to a divergence of 0.2 mrad [16], and an oxidized Si substrate mounted facing the atom beam. The standing wave, which grazes across the substrate surface with its maximum intensity at the surface, has a $1/e^2$ radius of 65 μm and is formed by retroreflecting a linearly-polarized laser beam through a quarter-wave plate. The single-beam

power was typically 20 mW. A single-frequency, stabilized ring-dye laser, operating at 425.43 nm (air wavelength) with stilbene 420 laser dye and pumped by a UV argon ion laser provides the laser light for both the optical collimation region and the standing wave. The dye laser is tuned 500 MHz above the atomic resonance to generate a standing wave with minimal probability of spontaneous emission. The atomic resonance utilized in the experiment is the $^7S_3 \rightarrow \, ^7P_4^o$ transition in chromium. The portion of the laser beam used for optical collimation is frequency-shifted by an acousto-optic modulator to about 5 MHz (one natural linewidth) below the atomic resonance. Three pairs of Helmholtz coils are used to cancel the earth's magnetic field to a level of about 2 μT.   After deposition of typically 20 minutes, the substrate is removed from vacuum and a "tapping-mode" atomic force micrograph of the chromium lines is made in air. Etched silicon tips with a nominal radius of 20 nm are used to image the lines, and the data shown are uncorrected for any effects due to the size or shape of the tips.

To generate a deposition profile, a series of line scans from an AFM image spanning a region 100 nm $\times$ 425 nm were band-averaged along the direction of the Cr lines. Fig. 2a shows such a band-averaged line scan for the *lin* $\perp$ *lin* optical field configuration. Clear $\lambda/8$ spacing is seen in the Cr lines, in very good agreement with the minimum spacing in the adiabatic potentials.

To further emphasize the importance of the adiabatic potentials, and to provide further evidence that the peaks in the deposited atomic distribution do arise from the avoided crossing minima in the potential, we varied the displacement between the two sets of adiabatic potentials by varying the angle φ between the polarizations of the two counterpropagating travelling waves. As φ is varied, the resulting optical field can be decomposed into two sets of oppositely

circularly polarized standing waves whose nodes are spatially displaced by $\Delta x = \varphi\,\lambda/2\pi$. Hence, we should expect the line spacing to vary from $\lambda/2$ to $\lambda/8$ as φ is varied from $\varphi = 0$, where there are no avoided crossings, to $\varphi = \pi/2$, where they are most pronounced. The linescans from AFM images of Cr lines deposited for several values of φ are shown in Fig. 2. The spacing of the structures is in excellent agreement with the expectations based on the spacings of the adiabatic optical potentials for the values of φ used. We note from a practical point of view that this provides a means of generating structures with a variable spacing, should this be desirable.

In order to analyze more accurately the behavior of the atoms in the *lin* $\perp$ *lin* light field, we have carried out a fully dynamical quantum calculation, in which the time-dependent Schrödinger equation is solved numerically. The internal degrees of freedom of the atom are set by the magnetic sublevels of the ground state, with $J_g = 3$, and the excited state, with $J_e = 4$, yielding a total number of 16 states. For the external degrees of freedom we tabulated the wave function in the momentum representation on a grid with 1 $\hbar$k spacing. Since the problem has a translational symmetry with periodicity λ, only momentum states which differ by n$\hbar$k are coupled to each other. Therefore the only approximation was the truncation at a finite maximum momentum, which was chosen to be much larger than the maximum momentum change during the laser interaction (120 $\hbar$k for the laser parameters as used in the experiment). For the propagation of the wave function we used a 4th-order Runge-Kutta method, which allowed us to also include the Gaussian turn-on of the laser intensity in the model.

The first goal of the theoretical analysis was to understand the role of nonadiabatic transitions in the formation of the $\lambda/8$ features. This could in principle be complicated by the fact that in addition to gaining kinetic energy in the potential wells, the atoms feel a time-

dependent potential because of their motion in the Gaussian shape of the laser beam. In order to concentrate only on the role of the potentials themselves, we first simulated the dynamics for a constant laser beam profile. Figs. 3a and 3c show the time evolution, averaged over space, of the populations of the adiabatic states for a Rabi frequency $\Omega = 4.8\times10^4\,\omega_{rec}$, where ω_{rec} is the recoil frequency, which is 22 kHz for chromium. In order to compare the dynamics in potential *1* to potential *2*, we chose either pure M = ±3 or M = ±2 states as initial Zeeman distributions.

Fig. 3a clearly shows the population in the *1*-state decaying over the course of interacting with the laser beam as a result of nonadiabatic transitions, as expected from the qualitative arguments discussed above. Fig. 3b shows the spatial probability distribution at the end of the interaction for the odd *M*-state family. Clearly there is no $\lambda/8$ component left. In Fig. 3c we see that the even *M*-state family populations remain essentially constant in time, indicating a very small probability of nonadiabatic transitions. As a result, the final spatial distribution for the even family, shown in Fig. 3d, shows a clear $\lambda/8$ component. Upon adding the effect of the Gaussian laser turn-on we saw only minor changes in the outcome, leading us to the conclusion that in this parameter regime the turn-on does not play a significant role in generating non-adiabatic effects.

The second goal of the theoretical study was to attempt to provide a comparision with the experimental results. To accomplish this, we solved the dynamics of the atomic motion in two steps. First we modeled the collimation of the atom by solving the optical Bloch equations for laser cooling by means of Quantum Monte Carlo simulations [17]. The resulting momentum distribution (Gaussian with rms width of 7 $\hbar$k) and the distribution in the ground state magnetic sublevels then served as an initial condition for the equation of motion in the localization region.

Although the laser parameters in the localization region ($\Omega = 7.0 \times 10^4 \, \omega_{rec}$; $\Delta = 2.3 \times 10^4 \, \omega_{rec}$) make conservative motion in the optical potentials the dominant interaction, we also had to include dissipative effects via a Monte Carlo approach. The probability for emitting a spontaneous photon in the localization region for the most probable velocity was calculated to be 0.37. We note that the impact of spontaneous emission on the motion does not come from the photon recoil, but from the redistribution into different magnetic states. Changing magnetic states corresponds to changing to a different optical potential, where the atom experiences a different force. The distribution in longitudinal velocities (Maxwellian distribution for a temperature of 1650° C) was taken into account by averaging over a distribution of interaction times and intensity profiles.

The result of the simulation is shown in Fig. 4, where qualitative agreement is seen with the experimental result of Fig. 2a. Clear peaks at odd multiples of $\lambda/8$ are seen in addition to the peaks at multiples of $\lambda/4$. The ratio of the height of the $\lambda/8$ peaks (largest contribution from level *2*) to the height of the $\lambda/4$ peaks (largest contribution from levels *6* and *7*) is 1:1.33, similar to the average experimental value of 1:1.18 ± 0.09. Differences between the calculation and the experiment in this ratio, and also in the line shapes, are not fully understood. Likely causes include the uncertainty in the initial conditions or exact position of the standing wave relative to the substrate. Also, AFM tip effects cannot be entirely ruled out. The small modulation in peak height with $\lambda/4$ periodicity in the experimental result is most likely a result of a population imbalance between magnetic substates due to stray magnetic fields in the interaction region.

We have used a new method for measuring the spatial distribution of atoms in a *lin* $\perp$ *lin* light field and explained the unexpectedly observed $\lambda/8$ periodicity. We found that the atomic

distribution in space is strongly influenced by avoided crossings in the optical potentials, and that nonadiabatic transitions in these crossings can be significant for near-resonant light fields. Further insight into the processes involved was gained by performing a fully dynamical quantum calculation. The level of complexity in atom-laser interactions unveiled in this study has provided new understanding, and we hope that this work will stimulate further work in this field.

References

1. See special issue J. Opt. Soc. Am. B **6**, 2020-2278 (1989).

2. See, *e.g.*, C. S. Adams, M. Sigel and J. Mlynek, Phys. Rep. **240**, 143 (1994).

3. S. L. Rolston and W. D. Phillips, Proceedings of the IEEE, **79**, 943 (1991) and references therein.

4. See special issues Appl. Phys. B **54**, 321-485 (1992) and J. de Physique, **4**, 1877-2097 (1994).

5. G. Timp *et al.*, Phys. Rev. Lett. **69**, 1636 (1992) and J. J. McClelland, *et al.*, Science **262**, 877 (1993).

6. P. S. Jessen *et al.*, Phys. Rev. Lett. **69,** 49 (1992).

7. P. Verkerk *et al.*, Phys. Rev. Lett. **68** 3861 (1992).

8. C. Salomon *et al.*, Phys. Rev. Lett. **59**, 1659 (1987).

9. J. E. Thomas, Opt. Lett. **14**, 1186 (1989).

10. G. Birkl *et al.*, Phys. Rev. Lett. **75** 2823 (1995).

11. P. Marte *et al*., Phys. Rev. Lett. **71**, 1335 (1993); R. Taïeb *et al*., Phys. Rev. A, **47**, 4986 (1993).

12. L. D. Landau, Phys. Z. Sowjetunion **1**, 89 (1932); C. Zener, Proc. Roy. Soc. London **137**, 696 (1932).

13. J.J. McClelland, R. Gupta, Z.J. Jabbour, and R.J. Celotta, Australian Journal of Physics (in press).

14. A. Zangwill, *Physics at Surfaces* (Cambridge Univ. Press, 1988), and A. Zangwill, private

communication.

15. R. E. Scholten *et al.*, J. Vac. Sci. Technol. B 12, 1847 (1994).

16. R. E. Scholten, R. Gupta, J. J. McClelland and R. J. Celotta, (to be published).

17. R. Dum, P. Zoller, and H. Ritsch, Phys. Rev. A 45, 4879 (1992) and J. Dalibard, Y. Castin, and K. Mölmer, Phys. Rev. Lett 68, 580 (1992).

Figure Captions

1. Adiabatic potentials in units of $E_{rec} \equiv \hbar\omega_{rec}$ (ω_{rec} is the recoil frequency, which is 22 KHz) for the $J_g=3 \rightarrow J_e=4$ transition in Cr, for an optical field consisting of two linear orthogonally-polarized travelling waves with a Rabi frequency of $\Omega=4.8\times10^4$ ω_{rec} and a detuning of $\Delta=2.3\times10^4$ ω_{rec}. (top) odd *M*-state family of potentials, (bottom) even *M*-state family of potentials. The potentials are numbered *1-7* for reference in the text.

2. Band-averaged atomic force linescans of Cr deposited on Si wafer in the presence of a *lin* ⊥ *lin* optical field, shown as a function of the angle φ between the linear polarizations of the two counterpropagating travelling waves. The value of φ are (a) 90° (b) 75° (c) 60° and (d) 0°. The vertical scale is set by the calibration of the atomic force microscope (accurate to ±10%), with the zero determined by measuring the height of a step formed by etching the sample. The zero is further corrected for a background of other isotopes (16%) and loss to Cr metastable ^{5}D states (estimated 7%).

3. Calculated population evolution and final spatial distribution for the various adiabatic states of Cr in a *lin* ⊥ *lin* optical field with constant profile. (a) Evolution of the odd *M*-sublevel family of states, averaged over space. Numbers correspond to the potentials in Fig. 1. (b) As in (a), for the even *M*-sublevel family of states. Time is expressed in units of T, one-fourth of the time period of oscillation in the optical potential for an atom with the most probable longitudinal

velocity. (c) The total spatial distribution for the atoms in the odd *M*-state family at t = T. (d) As in (c), for the even *M*-state family.

4. Quantum Monte Carlo calculation of the spatial distribution of Cr atoms traversing a *lin* ⊥ *lin* optical field, showing clear $\lambda/8$ features. All salient features of the experiment are taken into account, including a Gaussian laser profile with waist 65 μm ($1/e^2$), a peak Rabi frequency of $\Omega=7.0\times10^4\omega_{rec}$, and a detuning of $\Delta=2.3\times10^4\omega_{rec}$, ($\omega_{rec}$ is the recoil frequency for Cr, which is 22 kHz). Initial conditions include magnetic-level relative population weights of 0.5 (*M=+3,-3*), 0.35 (*M=+2,-2*), 0.1 (*M=+1,-1*) and 0.05 *(M=0)*, a Gaussian transverse velocity distribution with rms spread of 7 $\hbar$k and a Maxwellian longitudinal velocity distribution corresponding to a temperature of 1650 °C.

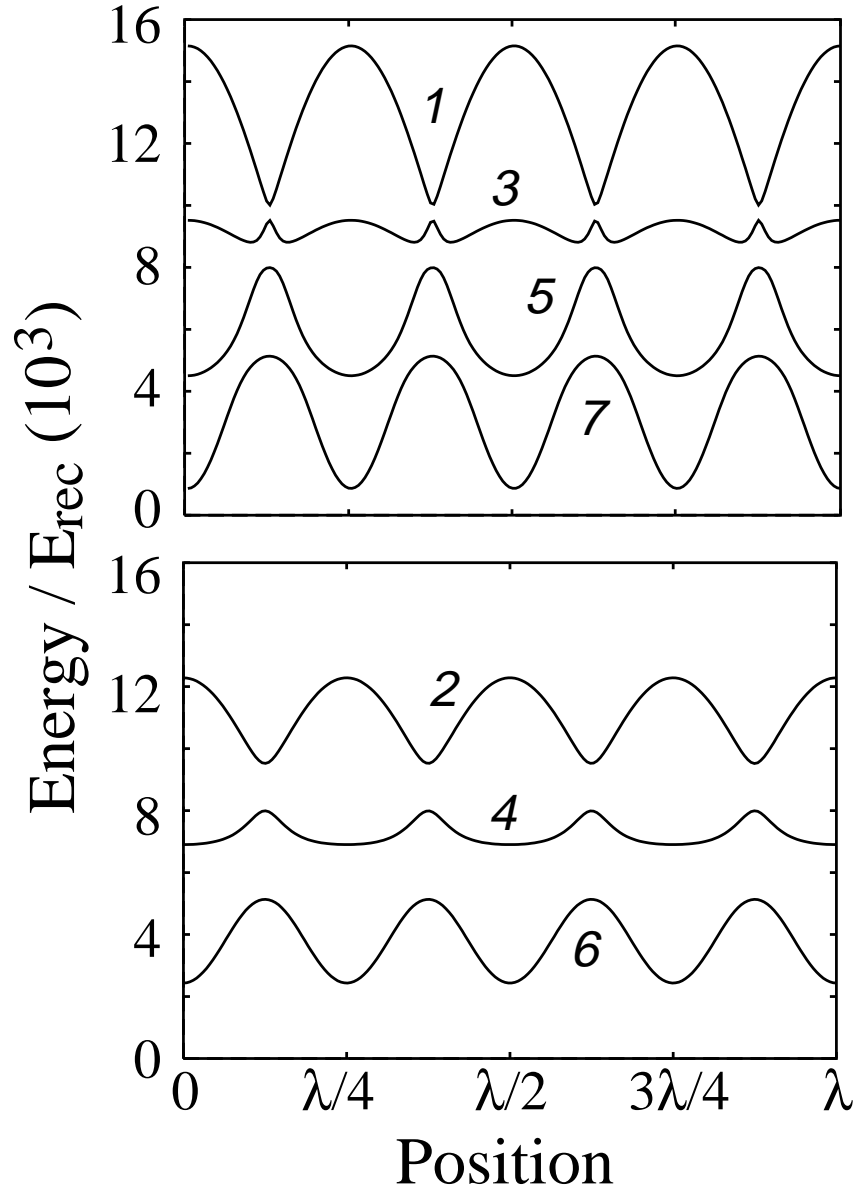**Figure 1** Adiabatic potentials in units of $E_{rec} \equiv \hbar\omega_{rec}$ (ω_{rec} is the recoil frequency, which is 22 KHz) for the $J_g=3 \rightarrow J_e=4$ transition in Cr, for an optical field consisting of two linear orthogonally-polarized travelling waves with a Rabi frequency of $\Omega=4.8\times10^4$ ω_{rec} and a detuning of $\Delta=2.310^4$ ω_{rec}. (top) odd *M*-state family of potentials, (bottom) even *M*-state family of potentials. The potentials are numbered *1-7* for reference in the text.
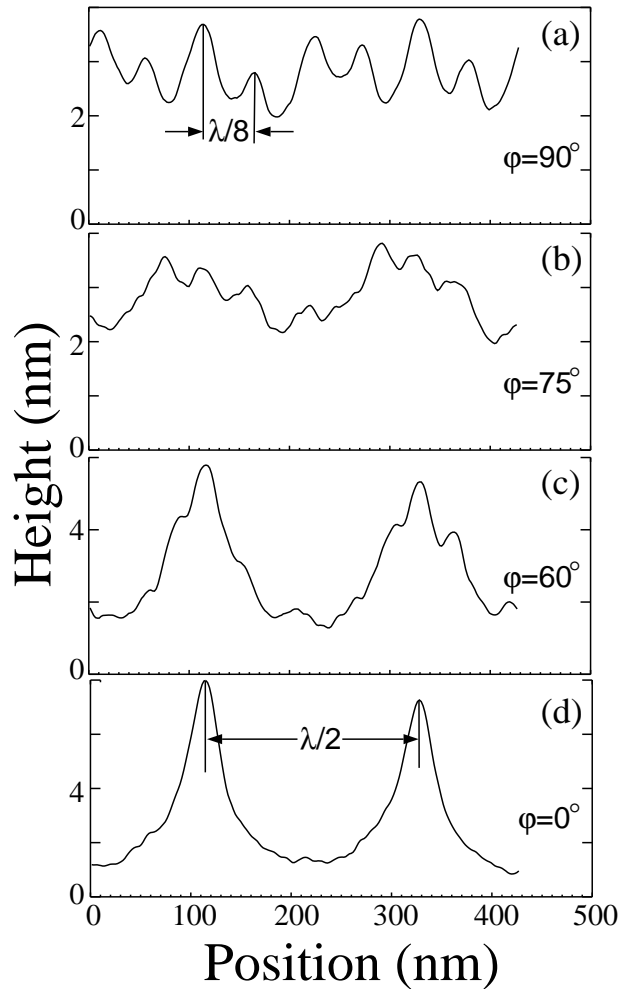
Figure 2 Band-averaged atomic force linescans of Cr deposited on Si wafer in the presence of a *lin △ lin* optical field, shown as a function of the angle φ between the linear polarizations of the two counterpropagating travelling waves. The value of φ are (a) 90° (b) 75° (c) 60° and (d) 0°. The vertical scale is set by the calibration of the atomic force microscope (accurate to ±10%), with the zero determined by measuring the height of a step formed by etching the sample. The zero is further corrected for a background of other isotopes (16%) and loss to Cr metastable ^5D states (estimated 7%).
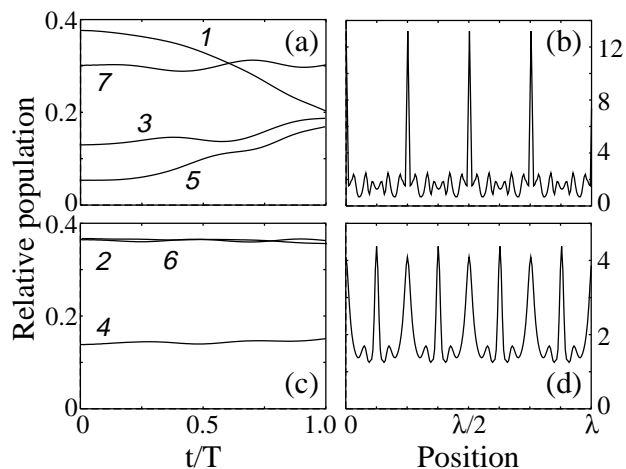
Figure 3 Calculated population evolution and final spatial distribution for the various adiabatic states of Cr in a *lin* ⊥ *lin* optical field with constant profile. (a) Evolution of the odd *M*-sublevel family of states, averaged over space. Numbers correspond to the potentials in Fig. 1. (b) As in (a), for the even *M*-sublevel family of states. Time is expressed in units of T, one-fourth of the time period of oscillation in the optical potential for an atom with the most probable longitudinal velocity. (c) The total spatial distribution for the atoms in the odd *M*-state family at t = T. (d) As in (c), for the even *M*-state family.
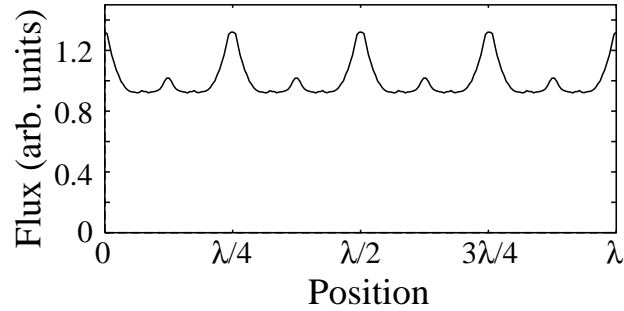
Figure 4 Quantum Monte Carlo calculation of the spatial distribution of Cr atoms traversing a *lin* $\perp$ *lin* optical field, showing clear $\lambda/8$ features. All salient features of the experiment are taken into account, including a Gaussian laser profile with waist 65 μm ($1/e^2$), a peak Rabi frequency of $\Omega=7.0\times10^4\omega_{rec}$, and a detuning of $\Delta=2.3\times10^4\omega_{rec}$, ($\omega_{rec}$ is the recoil frequency for Cr, which is 22 kHz). Initial conditions include magnetic-level relative population weights of 0.5 (*M*=+3,-3), 0.35 (*M*=+2,-2), 0.1 (*M*=+1,-1) and 0.05 *(M*=0), a Gaussian transverse velocity distribution with rms spread of 7 $\hbar$k and a Maxwellian longitudinal velocity distribution corresponding to a temperature of 1650 °C.